International Journal of Heat and Mass Transfer 80 (2015) 812–824

Contents lists available at ScienceDirect

International Journal of Heat and Mass Transfer

journal homepage: www.elsevier.com/locate/ijhmt

A unified coupling scheme between lattice Boltzmann method and finite volume method for unsteady fluid flow and heat transfer

Zi-Xiang Tong, Ya-Ling He *

Key Laboratory of Thermo-Fluid Science and Engineering of MOE, School of Energy and Power Engineering, Xi'an Jiaotong University, No. 28 Xianning West Road, Xi'an, Shaanxi 710049, PR China

ARTICLE INFO

Article history:
Received 14 May 2014
Received in revised form 24 September 2014
Accepted 25 September 2014
Available online 23 October 2014

Keywords:
Unsteady coupling scheme
Lattice Boltzmann method
Finite volume method
Generalized reconstruction operator
Natural convection
Flow around cylinder

ABSTRACT

In this paper, a unified coupling scheme between the lattice Boltzmann method (LBM) and the finite volume method (FVM) is proposed for the unsteady fluid flow and heat transfer problems. Three improvements are achieved comparing to the existing coupling methods. Firstly, a generalized form of the reconstruction operator (RO) is derived for the information transfer from macroscopic parameters to LBM distribution functions. The existing RO for various LBM can all be derived from this generalized form. Secondly, an RO corresponding to the incompressible LBM is derived to deal with the incompressible flow, which can prevent the inconsistency between the incompressible FVM and the density change in the LBM. Thirdly, the time coupling scheme between LBM and FVM is proposed for the unsteady simulations. The LBM and FVM are solving sequentially and the information is transferred between the two methods at the intervals. The coupling scheme is validated by three numerical examples: the convection–diffusion of a Gaussian pulse, the unsteady flow past a circular cylinder and the start-up process of the natural convection in a square cavity. The numerical results agree well with the existing researches. The flow past a porous medium is also simulated to show the application of the coupling method. This method can give the detailed flow information and save the computational time. The proposed coupling scheme improves and expands the coupling scheme between LBM and FVM. It has the flexibility to simulate unsteady multiscale processes.

1. Introduction

Many physical processes are multiscale in nature, such as the mass transfer in a fuel cell [1], the chemical vapor deposition on a thin film [2], the CO_2 sequestration [3] and the heat transfer in silica aerogel composite insulating materials [4]. In these "multiscale processes", the overall behaviors are dominated by several strongly coupled sub-processes which occur in different length and time scales and are always described by different governing equations [5]. The numerical simulations are efficient ways to study these complex problems and direct the experiments. However, since the traditional numerical methods always model the problems from a single scale, they are not suitable for the multiscale simulations. A numerical simulation from the large scale ignores the detailed local information which is often mostly concerned, while the large computational time consuming of a simulation from the small scale is also unacceptable [6]. Therefore, the new numerical methods are needed and the multiscale simulation methods are proposed.

The "Solving problems regionally and coupling at the interface [7]" is a widely used multiscale strategy, where the computational domain is divided into different sub-regions in which the most proper numerical methods are adopted as shown in Fig. 1. An overlapping region where both methods are adopted is located between the sub-regions for information transfer. A compression operator (CO) is employed at the macroscopic boundary for the information transfer from the micro/mesoscale to the macroscale and a reconstruction operator (RO) is adopted at the micro/mesoscopic boundary for the inverse information transfer [7]. Based on this strategy, many coupling methods between different numerical models have been proposed for various multiscale problems, such as molecular dynamic (MD)-continuum [8–13], direct simulation of Monte Carlo (DSMC)-continuum [14,15], and lattice Boltzmann method (LBM)-finite volume method (FVM) [16–21].

The research in this paper is focused on the coupling between the LBM and the FVM. The LBM has been developed into a useful method for multi-physical and multi-component problems [22,23]. It can be adopted to obtain the detailed information in the

* Corresponding author. Tel.: +86 29 82665930; fax: +86 29 82665445.
E-mail addresses: yalinghe@mail.xjtu.edu.cn, hylepe@gmail.com (Y.-L. He).

http://dx.doi.org/10.1016/j.ijheatmasstransfer.2014.09.067
0017-9310/

complex boundaries due to its flexibility [24] and the FVM can be adopted in the free area to speed up the computation [5]. This kind of coupling method has been used to simulate the lid-driven cavity flow [5], the natural convection [16], the flow around a circular cylinder, an airfoil, a porous medium [17] and the fluid flow and mass transfer in a proton exchange membrane fuel cell [18,19].

However, there are three shortages in the existing coupling methods.

Firstly, the ROs of different lattice Boltzmann (LB) models are derived separately. For example, the ROs for the density–velocity distribution functions and the concentration/temperature distribution functions have been derived separately in Refs. [16,18,19]. The applications of these ROs are limited because there are many other different LB models used in the numerical simulations and the new operators are needed. Meanwhile, the derivation procedures are not well summarized in the existing researches, so the derivations of the new operators may be complicated. Therefore, a generalized form of the RO is needed.

Secondly, in the LBM region, the lattice Boltzmann BGK (LBGK) model [24] is used to simulate the velocity field. Since the macroscopic equations recovered by the LBGK model are actually compressible [25,26], they are inconsistent with the incompressible equations used in the FVM. This leads to some troubles in the coupling. For example, the recovered compressible momentum equation introduces into the RO a term including the density gradient, although the density in the FVM region remains constant [16–21]. Consequently, the gradient of the pressure in the FVM region is used as a substitute since the pressure in the LBGK model is in proportion to the density [20]. The application of an incompressible LBM can resolve this mismatch.

Thirdly, all the above coupling methods between the LBM and the FVM are proposed for the steady problems and few researches have been published for the unsteady coupling method. This limits the application of these coupling methods since many problems are unsteady, not only the problems in the start-up stage or with time-variant boundary conditions, but also the problems at high Reynolds number (Re) such as the von Karman vortex street behind a circular cylinder when $Re > 40$ [27]. Therefore, the Re in the existing papers is relatively low [5]. The steady coupling method also causes an inconvenience in deriving the RO. The key point for the derivation of the RO is to calculate the distribution functions of the LBM by the values and the gradients of the macroscopic parameters. The unsteady nature of the LBM will inherently bring the time derivatives into the RO. However, since the time is not clearly defined in the steady coupling method, the time derivatives are replaced by the spatial derivatives according to the conservation equations [5,16–21]. This expedient inevitably complicates the derivation and elongates the expressions of the RO. A clear definition of the time in the coupling methods may preclude this inconvenience. Consequently, an unsteady coupling method between LBM and FVM is needed.

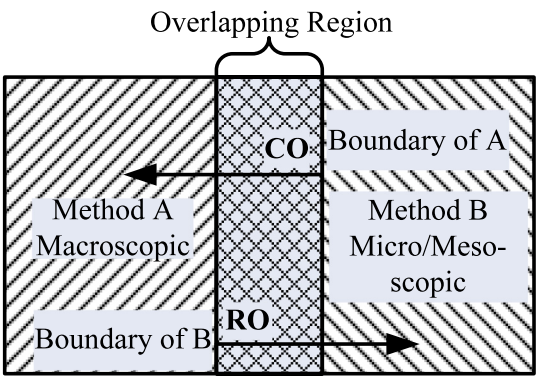

Fig. 1. Sketch of the computational domain of the coupling strategy "Solving problems regionally and coupling at the interfaces". CO is the compression operator and RO is the reconstruction operator.

As for the first problem, the derivation procedures of the RO can be divided into two parts. First part includes the common procedures which do not depend on the models, such as the Chapman–Enskog expansions and the chain rule of derivatives. The other part includes the procedures depend on the models such as the macroscopic equations at different scale and the partial derivatives of the distribution functions. In the existing derivations, the two parts are mixed. If we rearrange the derivations and carry out all the independent procedures before the dependent ones, the generalized form of the RO may be established.

The solution for the second problem is easy because the incompressible LBM already exists [25,26]. Once the generalized RO is obtained, the RO for the incompressible LBM will be derived without difficulty.

The third problem is more challenging because the boundary conditions vary with time at the boundaries of the overlapping region during the simulation. Some helpful references can be found in the coupling between the MD and the continuum methods. The MD simulates the motions of the individual molecules and calculates the macroscopic values by the time averages. It is also an unsteady method in nature which is similar to the LBM. Two types of the time coupling strategies are described by Delgado-Buscalioni and Coveney: the synchronized and sequential coupling [28]. The synchronized-coupling is a parallel strategy in which the two methods advance separately and exchange information at certain moments. In the sequential-coupling strategy, the MD firstly advances for a time interval Δt_c equal to that of the continuum method. Then the continuum method advances for Δt_c with the boundary conditions given by the above MD interval. The new solution of the continuum method is used as the boundary condition of the MD, and the above procedures are repeated. The sequential-coupling strategy is employed in many researches [11–13,29]. Therefore, a similar time coupling strategy will be used in the present work to deal with the unsteady problems.

The rest of the paper is organized as follows. In Section 2, the incompressible LBM and FVM are briefly described. Then, the generalized RO is derived in Section 3 and the existing ROs are also derived from this generalized form. In Section 4, the RO for the incompressible LBM is derived and the unsteady coupling scheme is described. Finally, the numerical examples are simulated in Section 5 and some conclusions are given in Section 6.

2. Brief introduction of the FVM and the incompressible LBM

2.1. Finite volume method

The macroscopic conservation equations are the bases of the FVM. In the present work, the fluid is assumed to be incompressible and the thermal diffusivity and viscosity are constants. The conservations of mass and momentum are given by

$$\nabla \cdot \mathbf{u} = 0 \tag{1}$$

$$\frac{\partial \mathbf{u}}{\partial t} + \nabla \cdot (\mathbf{u}\mathbf{u}) = -\nabla P + \nu \nabla^2 \mathbf{u} \tag{2}$$

and the energy conservation is given by

$$\frac{\partial T}{\partial t} + \nabla \cdot (\mathbf{u}T) = \alpha \nabla^2 T \tag{3}$$

Here $\mathbf{u}$ is the velocity, t is the time, P is the kinematic pressure, T is the temperature, ν is the kinematic viscosity and α is the thermal diffusivity.

In this paper, The SIMPLE algorithm [30,31] is used to solve these equations. The fully implicit scheme is used for the time

discretization and the power-law scheme is used for the discretization of the convective term [30,31].

2.2. Incompressible lattice Boltzmann method for fluid flow and heat transfer

In the present paper, the double-distribution-function model is used to simulate the fluid flow and heat transfer [26]. The incompressible LBM which can recover Eqs. (1) and (2) is adopted for the velocity field [25,26] and the evolution equation is

$$f_i(\mathbf{x}+\mathbf{e}_i\Delta t, t+\Delta t) - f_i(\mathbf{x},t) = -\frac{f_i(\mathbf{x},t) - f_i^{eq}(\mathbf{x},t)}{\tau_v} \tag{4}$$

in which $f_i(\mathbf{x},t)$ is the ith density distribution function at spatial location $\mathbf{x}$ and time t. The D2Q9 model [32] is adopted for the discrete velocities $\mathbf{e}_i$ as

$$\mathbf{e}_i = \begin{cases} 0 & i=0 \\ c(\cos[(i-1)\pi/2], \sin[(i-1)\pi/2]) & i=1,2,3,4 \\ c(\cos[(i-1)\pi/2+\pi/4], \sin[(i-1)\pi/2+\pi/4]) & i=5,6,7,8 \end{cases} \tag{5}$$

where the lattice speed c is equal to $\Delta x/\Delta t$ (Δx and Δt are the space and time interval in the simulation).

The relaxation time τ_v is related to the kinematic viscosity v via

$$v = c^2(2\tau_v - 1)\Delta t/6 \tag{6}$$

The equilibrium distribution functions can be written as [25]

$$f_i^{eq}(\mathbf{x},t) = \xi_i \frac{P}{c^2} + w_i\left[3\frac{\mathbf{e}_i\cdot\mathbf{u}}{c^2} + \frac{9}{2}\frac{(\mathbf{e}_i\cdot\mathbf{u})^2}{c^4} - \frac{3}{2}\frac{u^2}{c^2}\right] \tag{7}$$

in which the weight parameters are $w_0 = 4/9$, $w_{1-4} = 1/9$, $w_{5-8} = 1/36$, $\xi_0 = -5/3$, $\xi_{1-4} = 1/3$ and $\xi_{5-8} = 1/12$. The kinematic pressure P and the velocity $\mathbf{u}$ are calculated by [25]

$$P = \frac{3c^2}{5}\left[\sum_{i=1}^{8} f_i - \frac{2}{3}\frac{u^2}{c^2}\right] \tag{8}$$

$$\mathbf{u} = \sum_{i=0}^{8} \mathbf{e}_i f_i \tag{9}$$

Another temperature distribution function $h_i(\mathbf{x},t)$ is adopted for the heat transfer and the evolution equation is

$$h_i(\mathbf{x}+\mathbf{e}_i\Delta t, t+\Delta t) - h_i(\mathbf{x},t) = -\frac{h_i(\mathbf{x},t) - h_i^{eq}(\mathbf{x},t)}{\tau_k} \tag{10}$$

where only the discrete velocities $\mathbf{e}_1$, $\mathbf{e}_2$, $\mathbf{e}_3$ and $\mathbf{e}_4$ are used and the equilibrium distribution function is given by [26]

$$h_i^{eq}(\mathbf{x},t) = \frac{T}{4}\left[1 + 2\frac{\mathbf{e}_i\cdot\mathbf{u}}{c^2}\right] \tag{11}$$

The temperature is calculated by the sum of the h_i as

$$T = \sum_{i=1}^{4} h_i \tag{12}$$

The thermal diffusivity is given by

$$\alpha = c^2(2\tau_k - 1)\Delta t/4 \tag{13}$$

3. Generalized form of the reconstruction operator

As mentioned in the introduction, the information exchanges between the LBM and FVM are carried out by the CO and RO at the boundaries. The LBM contains more information because all the distribution functions at each node are computed instead of the macroscopic parameters $\mathbf{u}$, P and T. Consequently, although the CO for the information transfer from LBM to FVM is simply given by Eqs. (8), (9) and (12), the RO for the opposite information transfer is complicated. Therefore, a generalized RO is needed which can be used to derive ROs for different LB models. In this section, we summarize all the derivation procedures which are not dependent on the LB models and derive the generalized form of the RO. The existing operators are also derived from the generalized form as examples.

3.1. Derivation of the generalized form of the reconstruction operator

As shown in Eqs. (4) and (10), the evolution equations of the LB models have a same form as

$$g_i(\mathbf{x}+\mathbf{e}_i\Delta t, t+\Delta t) - g_i(\mathbf{x},t) = -\frac{g_i(\mathbf{x},t) - g_i^{eq}(\mathbf{Y}(\mathbf{x},t))}{\tau} \tag{14}$$

where g_i is the distribution function. The equilibrium distribution function g_i^{eq} is the function of $\mathbf{Y}(\mathbf{x},t)$ which is a vector composed of all the macroscopic parameters. $\mathbf{Y}(\mathbf{x},t)$ varies with the location and time. For example, $\mathbf{Y}$ equals $[P,u,v]$ for the incompressible model and $[T,u,v]$ for the heat transfer model. The τ is the relaxation time. The derivation of the generalized form of RO is as follows.

(1) The Chapman–Enskog multiscale expansions.
The time and space scale can be expanded as

$$\frac{\partial}{\partial t} = \varepsilon\frac{\partial}{\partial t^{(1)}} + \varepsilon^2\frac{\partial}{\partial t^{(2)}} \tag{15}$$

$$\nabla = \varepsilon\nabla^{(1)} \tag{16}$$

in which ε is a small parameter. The distribution function is expanded as

$$g_i = g_i^{(0)} + \varepsilon g_i^{(1)} + \varepsilon^2 g_i^{(2)} \tag{17}$$

The evolution Eq. (14) is expanded about $\mathbf{x}$, t and the equations at different scale ε^0, ε^1, ε^2 are obtained as

$$\varepsilon^0 : g_i^{(0)} = g_i^{eq} \tag{18}$$

$$\varepsilon^1 : g_i^{(1)} = -\Delta t\tau\left(\frac{\partial}{\partial t^{(1)}} + \mathbf{e}_i\cdot\nabla^{(1)}\right)g_i^{eq} \tag{19}$$

$$\varepsilon^2 : g_i^{(2)} = -\tau\Delta t\frac{g_i^{eq}}{\partial t^{(2)}} - \tau\Delta t^2\left(\frac{1}{2}-\tau\right)\left(\frac{\partial}{\partial t^{(1)}} + \mathbf{e}_i\cdot\nabla^{(1)}\right)^2 g_i^{eq} \tag{20}$$

As indicated by Eqs. (17) and (18), the distribution function g_i is divided into the equilibrium component g_i^{eq} and the non-equilibrium components $g_i^{(1)}$, $g_i^{(2)}$ at different scale. The g_i^{eq} is a given function such as Eqs. (7) and (11), but the $g_i^{(1)}$ and $g_i^{(2)}$ are given by relatively complex Eqs. (19) and (20), which are composed of the space and time derivatives of the g_i^{eq}. Therefore, the main purpose of the following procedures is to represent these derivatives by the macroscopic parameters.

(2) Combine equilibrium and non-equilibrium components.
Substituting Eqs. (19) and (20) into Eq. (17), we have

$$\begin{aligned} g_i &= g_i^{eq} - \Delta t\tau\left(\varepsilon\frac{\partial}{\partial t^{(1)}} + \mathbf{e}_i\cdot\varepsilon\nabla^{(1)}\right)g_i^{eq} - \tau\Delta t\varepsilon^2\frac{g_i^{eq}}{\partial t^{(2)}} \\ &\quad - \tau\Delta t^2\left(\frac{1}{2}-\tau\right)\varepsilon^2\left(\frac{\partial}{\partial t^{(1)}} + \mathbf{e}_i\cdot\nabla^{(1)}\right)^2 g_i^{eq} \\ &= g_i^{eq} - \Delta t\tau\left[\left(\frac{\partial}{\partial t} + \mathbf{e}_i\cdot\nabla\right)g_i^{eq} - \Delta t\left(\frac{1}{2}-\tau\right)\left(\varepsilon\frac{\partial}{\partial t^{(1)}} + \mathbf{e}_i\cdot\nabla\right)^2 g_i^{eq}\right] \\ &\approx g_i^{eq} - \Delta t\tau D_i g_i^{eq} \end{aligned} \tag{21}$$

Here the Eqs. (15), (16) and the following concise expressions are used.

$$D_i = \frac{\partial}{\partial t} + \mathbf{e}_i\cdot\nabla \tag{22}$$

The second-order derivatives of g_i^{eq} are ignored as in the existing researches [5,16,18].

(3) Expressions of the derivatives of g_i^{eq}
The derivatives of the distribution functions are replaced by the derivatives of the macroscopic parameters by the chain rule:

$$D_i g_i^{eq} = \frac{\partial g_i^{eq}}{\partial \mathbf{Y}} D_i \mathbf{Y} = \sum_{k=1}^{N} \frac{\partial g_i^{eq}}{\partial Y_k} D_i Y_k \tag{23}$$

Here N denotes the number of the macroscopic parameters.

(4) The generalized form of reconstruction operator

By substituting Eq. (23) into Eq. (21), we finally get the generalized form of RO as

$$g_i = g_i^{eq} - \Delta t\tau \frac{\partial g_i^{eq}}{\partial \mathbf{Y}} D_i \mathbf{Y} = g_i^{eq} - \Delta t\tau \sum_{k=1}^{N} \frac{\partial g_i^{eq}}{\partial Y_k} D_i Y_k \tag{24}$$

Eq. (24) is derived from the general form of the evolution equation for all the LBM and no assumption about a specific model is introduced. Once the LB model is specified, the partial derivatives of g_i^{eq} are obtained straightforwardly. The derivatives of the macroscopic parameters are calculated by the finite differences of the results of the macroscopic methods. The time derivatives can be replaced by the spatial derivatives according to the macroscopic equations of the LBM, which always already exist.

Comparing with the existing derivations [5,16–21], the above derivations collect all the procedures which have no relation with the specific LB model. In the existing derivations, the expressions for $g_i^{(1)}$, $g_i^{(2)}$ are derived completely before the combination in the procedure 2. The chain rule is used in Eqs. (19) and (20) for the derivatives of g_i^{eq} at different scales. Therefore, the derivatives of the macroscopic parameters at different scales are introduced. In order to obtain these derivatives, the macroscopic equations of the LBM at different scales are derived from the sum of the Eqs. (19) and (20) over velocity space. This operation occupies a certain length in the existing derivations. The above derivation demonstrates that this operation is not necessary, because the derivatives of g_i^{eq} at different scales can be summed up in advance as shown in Eq. (21). In order to validate the generalized form (24) and show its application, we derive the existing ROs from Eq. (24).

3.2. Derivations of the existing reconstruction operators

3.2.1. Reconstruction operator for LBGK model

The LBGK model is used in Refs. [5,16–21], where the derivatives of the equilibrium distribution functions are calculated by

$$\frac{\partial f_i^{eq}}{\partial \rho} = \frac{f_i^{eq}}{\rho} \tag{25}$$

$$\frac{\partial f_i^{eq}}{\partial u_\beta} = \frac{U_{i\beta}}{c_s^2} f_i^{eq} \tag{26}$$

where β denotes the direction of the velocity, $c_s = c/\sqrt{3}$ is the speed of sound in LBM and $U_{i\beta} = e_{i\beta} - u_\beta$. The macroscopic equations corresponding to the LBGK model are [33,34]

$$\frac{\partial \rho}{\partial t} + \frac{\partial \rho u_\alpha}{\partial x_\alpha} = 0 \tag{27}$$

$$\rho\left(\frac{\partial u_\beta}{\partial t} + u_\alpha \frac{\partial u_\beta}{\partial x_\alpha}\right) = -\frac{\partial (c_s^2 \rho)}{\partial x_\beta} + \nu \frac{\partial}{\partial x_\alpha}(\rho S_{\alpha\beta}) \tag{28}$$

$$S_{\alpha\beta} = \frac{\partial u_\beta}{\partial x_\alpha} + \frac{\partial u_\alpha}{\partial x_\beta} \tag{29}$$

Here the summation is performed over repeated index α. This summation convention is used in the following of this work. Substituting Eqs. (25) and (26) into Eq. (24), we have

$$\begin{aligned} f_i &= f_i^{eq} - \Delta t\tau\left[\frac{\partial f_i^{eq}}{\partial \rho}\left(\frac{\partial \rho}{\partial t} + e_{i\alpha}\frac{\partial \rho}{\partial x_\alpha}\right) + \frac{\partial f_i^{eq}}{\partial u_\beta}\left(\frac{\partial u_\beta}{\partial t} + e_{i\alpha}\frac{\partial u_\beta}{\partial x_\alpha}\right)\right] \\ &= f_i^{eq} - \Delta t\tau\left[\frac{f_i^{eq}}{\rho}\left(\frac{\partial \rho}{\partial t} + e_{i\alpha}\frac{\partial \rho}{\partial x_\alpha}\right) + \frac{U_{i\beta}}{c_s^2} f_i^{eq}\left(\frac{\partial u_\beta}{\partial t} + e_{i\alpha}\frac{\partial u_\beta}{\partial x_\alpha}\right)\right] \\ &= f_i^{eq}\left\{1 - \Delta t\tau\left[\left(\frac{\partial \rho}{\rho \partial t} + \frac{e_{i\alpha}}{\rho}\frac{\partial \rho}{\partial x_\alpha}\right) + \frac{U_{i\beta}}{c_s^2}\left(\frac{\partial u_\beta}{\partial t} + e_{i\alpha}\frac{\partial u_\beta}{\partial x_\alpha}\right)\right]\right\} \end{aligned} \tag{30}$$

Then the Eqs. (27) and (28) are used to replace the time derivatives with the spatial derivatives, and the divergence-free assumption $\nabla \cdot \mathbf{u} = 0$ is used.

$$\begin{aligned} f_i &= f_i^{eq}\left\{1 - \Delta t\tau\left[\left(-\frac{\partial \rho u_\alpha}{\rho \partial x_\alpha} + \frac{e_{i\alpha}}{\rho}\frac{\partial \rho}{\partial x_\alpha}\right) + \frac{U_{i\beta}}{c_s^2}\left(\frac{\nu \partial}{\rho \partial x_\alpha}(\rho S_{\alpha\beta}) - \frac{\partial (c_s^2 \rho)}{\rho \partial x_\beta} - u_\alpha \frac{\partial u_\beta}{\partial x_\alpha} + e_{i\alpha}\frac{\partial u_\beta}{\partial x_\alpha}\right)\right]\right\} \\ &= f_i^{eq}\left\{1 - \Delta t\tau\left[\frac{U_{i\beta}}{\rho}\frac{\partial \rho}{\partial x_\alpha} + \frac{U_{i\beta}}{c_s^2}\left(\frac{\nu \partial}{\rho \partial x_\alpha}(\rho S_{\alpha\beta}) - \frac{\partial (c_s^2 \rho)}{\rho \partial x_\beta} + U_{i\alpha}\frac{\partial u_\beta}{\partial x_\alpha}\right)\right]\right\} \\ &= f_i^{eq}\left[1 - \frac{\Delta t\tau U_{i\beta}}{c_s^2}\left(\nu\frac{\partial S_{\alpha\beta}}{\partial x_\alpha} + \frac{\nu S_{\alpha\beta}}{\rho}\frac{\partial \rho}{\partial x_\alpha} + U_{i\alpha}\frac{\partial u_\beta}{\partial x_\alpha}\right)\right] \\ &= f_i^{eq}\left[1 - \frac{\Delta t\tau U_{i\beta}}{c_s^2}\left(\nu\nabla^2 u_\beta + \frac{\nu S_{\alpha\beta}}{\rho}\frac{\partial \rho}{\partial x_\alpha} + U_{i\alpha}\frac{\partial u_\beta}{\partial x_\alpha}\right)\right] \end{aligned} \tag{31}$$

Eq. (31) is the same as the RO for the density-velocity distribution functions in Refs. [5,16–21].

3.2.2. Reconstruction operator for the temperature

As for the temperature distribution functions used in Ref. [16], the derivatives are as follows

$$\frac{\partial g_i^{eq}}{\partial T} = \frac{g_i^{eq}}{T} \tag{32}$$

$$\frac{\partial g_i^{eq}}{\partial u_\beta} = \frac{w_i e_{i\beta} T}{c_s^2} \tag{33}$$

Substituting Eqs. (32) and (33) into the generalized RO, we obtain

$$g_i = g_i^{eq} - \Delta t\tau_g\left(\frac{g_i^{eq}}{T}\left(\frac{\partial T}{\partial t} + e_{i\alpha}\frac{\partial T}{\partial x_\alpha}\right) + \frac{w_i e_{i\beta} T}{c_s^2}\left(\frac{\partial u_\beta}{\partial t} + e_{i\alpha}\frac{\partial u_\beta}{\partial x_\alpha}\right)\right) \tag{34}$$

Then, the macroscopic equation for temperature (3) and the momentum Eq. (28) are used along with $\nabla \cdot \mathbf{u} = 0$.

$$\begin{aligned} g_i &= g_i^{eq} - \Delta t\tau_g\left[\frac{g_i^{eq}}{T}\left(\alpha\nabla^2 T - \frac{u_\alpha \partial T}{\partial x_\alpha} + \frac{e_{i\alpha}\partial T}{\partial x_\alpha}\right) + \frac{w_i e_{i\beta} T}{c_s^2}\left(\nu\nabla^2 u_\beta + \frac{\nu S_{\alpha\beta}}{\rho}\frac{\partial \rho}{\partial x_\alpha} + U_{i\alpha}\frac{\partial u_\beta}{\partial x_\alpha} - \frac{c_s^2 \partial \rho}{\rho \partial x_\beta}\right)\right] \\ &= g_i^{eq} - \Delta t\tau_g\left[\frac{g_i^{eq}}{T}\left(\alpha\nabla^2 T + U_{i\alpha}\frac{\partial T}{\partial x_\alpha}\right) + \frac{w_i e_{i\beta} T}{c_s^2}\frac{c_s^2}{\Delta t\tau U_{i\beta}}\frac{(f_i^{eq} - f_i)}{f_i^{eq}} - \frac{w_i e_{i\beta} T}{\rho}\frac{\partial \rho}{\partial x_\beta}\right] \\ &= g_i^{eq}\left[1 - \frac{\Delta t\tau_g}{T}\left(\alpha\nabla^2 T + U_{i\alpha}\frac{\partial T}{\partial x_\alpha}\right)\right] - \frac{w_i e_{i\beta} T\tau_g}{\tau U_{i\beta}}\frac{(f_i^{eq} - f_i)}{f_i^{eq}} + \frac{\Delta t\tau_g w_i e_{i\beta} T}{\rho}\frac{\partial \rho}{\partial x_\beta} \end{aligned} \tag{35}$$

Eq. (35) is the same as the RO used in Ref. [16].

3.2.3. General reconstruction operator for scalar convection–diffusion equations

Chen et al. have proposed a RO for the concentration distribution functions [18,19] and further developed it to all the scalars φ which are described by the following convection–diffusion equations [20]

$$\frac{\partial \varphi}{\partial t} + \mathbf{u} \cdot \nabla \varphi = \Gamma \nabla^2 \varphi \tag{36}$$

The derivatives of the distribution functions are

$$\frac{\partial g_i^{eq}}{\partial \varphi} = \frac{g_i^{eq}}{\varphi} \tag{37}$$

$$\frac{\partial g_i^{eq}}{\partial u_\beta} = \frac{\varphi}{2} e_{i\beta} \tag{38}$$

Therefore, the RO is given by

$$\begin{aligned} g_i &= g_i^{eq} - \Delta t \tau_\varphi \left(\frac{g_i^{eq}}{\varphi} \left(\frac{\partial \varphi}{\partial t} + e_{i\alpha} \frac{\partial \varphi}{\partial x_\alpha} \right) + \frac{\varphi e_{i\beta}}{2} \left(\frac{\partial u_\beta}{\partial t} + e_{i\alpha} \frac{\partial u_\beta}{\partial x_\alpha} \right) \right) \\ &= g_i^{eq} - \Delta t \tau_\varphi \left[\frac{g_i^{eq}}{\varphi} \left(\Gamma \nabla^2 \varphi - \frac{u_\alpha \partial \varphi}{\partial x_\alpha} + \frac{e_{i\alpha} \partial \varphi}{\partial x_\alpha} \right) \right. \\ &\quad \left. + \frac{\varphi e_{i\beta}}{2} \left(\nu \nabla^2 u_\beta + \frac{\nu S_{\alpha\beta}}{\rho} \frac{\partial \rho}{\partial x_\alpha} + U_{i\alpha} \frac{\partial u_\beta}{\partial x_\alpha} - \frac{c_s^2 \partial \rho}{\rho \partial x_\beta} \right) \right] \\ &= g_i^{eq} \left[1 - \frac{\Delta t \tau_\varphi}{\varphi} \left(\Gamma \nabla^2 T + \frac{U_{i\alpha} \partial T}{\partial x_\alpha} \right) \right] \\ &\quad - \frac{\tau_\varphi \Delta t \varphi e_{i\beta}}{2} \left(\nu \nabla^2 u_\beta + \frac{\nu S_{\alpha\beta} \partial \rho}{\rho \partial x_\alpha} + \frac{U_{i\alpha} \partial u_\beta}{\partial x_\alpha} \right) + \frac{\tau_\varphi \Delta t \varphi e_{i\beta} c_s^2}{2\rho} \frac{\partial \rho}{\partial x_\beta} \end{aligned} \tag{39}$$

which is the same as the RO in Refs. [18–20].

Therefore, the existing ROs can be derived from the generalized form. This proves that the generalized form can be used in deriving the RO for different LB models.

4. Coupling scheme

In this section, the ROs for the incompressible LBM and the temperature are derived. Then, the time coupling scheme for the unsteady problems is described.

4.1. Reconstruction operators for incompressible LBM and temperature

As for the equilibrium distribution function (7), the partial derivatives are

$$\frac{\partial f_i^{eq}}{\partial P} = \frac{\xi_i}{c^2} \tag{40}$$

$$\frac{\partial f_i^{eq}}{\partial u_\beta} = w_i \left(\frac{3U_\beta}{c^2} + \frac{9 e_{i\alpha} u_\alpha}{c^4} e_{i\beta} \right) \tag{41}$$

Substituting the above equations into Eq. (24), the following RO for the incompressible LBM is obtained.

$$\begin{aligned} f_i = f_i^{eq} - \Delta t \tau_v \left[\frac{\xi_i}{c^2} \left(\frac{\partial P}{\partial t} + e_{i\alpha} \frac{\partial P}{\partial x_\alpha} \right) + w_i \left(\frac{3U_\beta}{c^2} + \frac{9 e_{i\alpha} u_\alpha}{c^4} e_{i\beta} \right) \right. \\ \left. \cdot \left(\frac{\partial u_\beta}{\partial t} + e_{i\alpha} \frac{\partial u_\beta}{\partial x_\alpha} \right) \right] \end{aligned} \tag{42}$$

As for the temperature distribution function (11), we have

$$\frac{\partial h_i^{eq}}{\partial T} = \frac{h_i^{eq}}{T} \tag{43}$$

$$\frac{\partial h_i^{eq}}{\partial u_\beta} = \frac{T e_\beta}{2c^2} \tag{44}$$

The RO for the temperature is similar to Eq. (34) as

$$h_i = h_i^{eq} - \Delta t \tau_k \left[\frac{h_i^{eq}}{T} \left(\frac{\partial T}{\partial t} + e_{i\alpha} \frac{\partial T}{\partial x_\alpha} \right) + \frac{T e_\beta}{2c^2} \cdot \left(\frac{\partial u_\beta}{\partial t} + e_{i\alpha} \frac{\partial u_\beta}{\partial x_\alpha} \right) \right] \tag{45}$$

The comparison between Eqs. (42) and (31) shows that the time derivatives may simplify the expression of the RO. If the derivation procedures similar to Eq. (31) are adopted in Eq. (42), the time derivative $\partial \mathbf{u}/\partial t$ will be replaced by three space derivatives $\nabla \cdot (\mathbf{uu})$, ∇P and $\nabla^2 \mathbf{u}$ according to the momentum equation (2), so the second-order derivatives will be introduced. Moreover, there is even no counterpart for $\partial P/\partial t$ in the macroscopic equations, so this term will be ignored in the steady method.

4.2. Time coupling scheme

In this section, the computational domain is similar to Fig. 1. The FVM is adopted in the left sub-region and the LBM is adopted in the right sub-region. An overlapping region is located between the two sub-regions where both the FVM and LBM are adopted. A sketch of the grid in the overlapping region is shown in Fig. 2. In the present work, the grids of the FVM and LBM regions coincide with each other in the overlapping region. However, the nodes of the two sub-regions are staggered. The nodes in the LBM region locate at the intersections of the grid lines, but the nodes in the FVM region locate at the center of the control volumes divided by the grid lines. Therefore, the interpolation should be employed at the boundaries. In the present work, a linear interpolation is adopted to calculate the values at the FVM boundary nodes from the north and south LBM nodes. A bilinear interpolation is used to get the macroscopic values at the LBM boundary nodes from the four neighboring FVM nodes. Then, the ROs are employed at the boundary to obtain the boundary conditions of the LBM region.

As for the time coupling scheme, the time interval in the LBM is denoted by Δt, and the time interval Δt^C in the FVM is m times as long as Δt ($\Delta t^C = m\Delta t$).

One way to establish the unsteady coupling scheme is to expand the steady coupling scheme [5,16–21] to the unsteady problems. In the steady coupling schemes, the time derivatives in the ROs (42) and (45) are replaced by the spatial derivatives. The information at the boundary is exchanged by the CO and RO as the boundary condition. The FVM and LBM are calculated alternately until the convergence is achieved in the entire region. The extension of the steady scheme to the unsteady scheme is straightforward, in which the fully implicit scheme is used in the FVM for the time interval Δt^C. When the results at time point $n\Delta t^C$ are known, the above coupling scheme can be used to obtain the results at $(n+1)\ \Delta t^C$. This procedure is employed in all the time steps successively and the unsteady problems can be solved. However, we do not choose this method because of the following two reasons. Firstly, as mentioned in Section 4.1, the replacement of the time derivatives may complicate the RO. Secondly, in order to obtain the convergent results at each time point, the FVM and LBM should be calculated alternately for several times, which consume a lot of computational time. In this kind of coupling scheme, the fully implicit scheme in the FVM can be regarded as the controller for the time evolution. However, since the LBM is an unsteady method in nature, we can regard the time in the LBM as a natural clock and let the LBM lead the time evolution. Therefore, the time coupling scheme used in the present work is sketched in Fig. 3. The procedures are described in detail as follows.

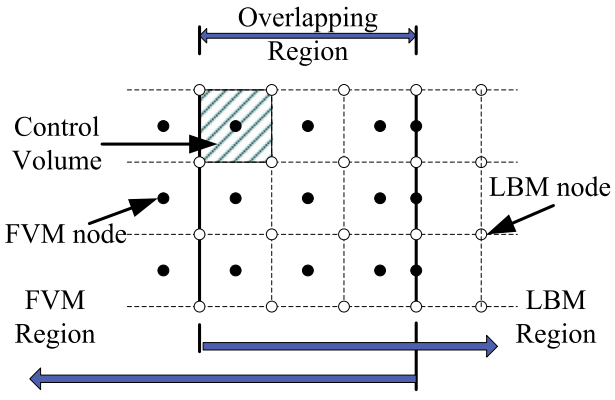

Fig. 2. The sketch of the grid in the overlapping region.

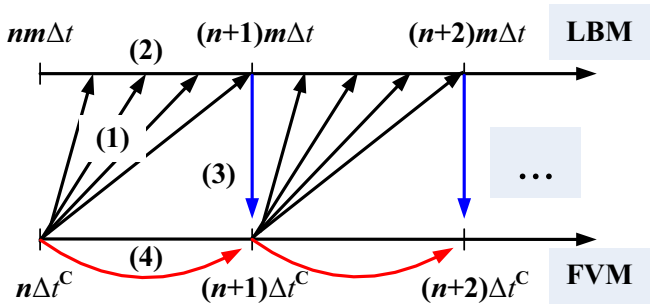

Fig. 3. The time coupling scheme.

(1) Reconstruction: We assume that the LBM and FVM results at the time $nm\Delta t$ ($n\Delta t^C$) are known. The ROs are adopted at the boundary of the LBM region to convert the macroscopic parameters to the distribution functions as the boundary conditions. Since the macroscopic parameters after $nm\Delta t$ are unknown, an extrapolation should be used for each LBM time point between $nm\ \Delta t$ and $(n+1)m\Delta t$. In the present work, when the boundary distribution functions at $nm\Delta t$ are obtained, the boundary conditions at the unknown time points are calculated by the second-order polynomial extrapolation with the distribution functions at time $nm\Delta t$, $(n-1)m\Delta t$ and $(n-2)m\Delta t$. The time derivatives in Eqs. (42) and (45) are also calculated by the second-order backward difference with the boundary values at the above three time points. The spatial derivatives are calculated by the central difference.

(2) LBM: The LBM is adopted in its sub-region with the boundary conditions calculated for each time point between $nm\Delta t$ and $(n+1)m\Delta t$. In this procedure, the LBM evolves m times. In the present work, m is close to the length of the LBM region to let the influence of the boundary condition at the coupling boundary propagate through the whole LBM region.

(3) Compression: Eqs. (9) and (12) are used at the FVM boundary to convert the distribution functions to the macroscopic parameters as the boundary conditions. In the present work, the velocity boundary is employed for the FVM, so the velocities at the FVM boundary are calculated and transferred. Here the time points $(n+1)m\Delta t$ and $(n+1)\Delta t^C$ for the two methods coincide with each other and no special treatment of the time is needed. However, in our numerical practice, we find that there are two problems in the FVM region which need special treatments: the mass conservation and the absolute value of the pressure. Firstly, as shown in the mass conservation equation (1) of the incompressible fluid, for an enclosed region, the integration of the velocity components normal to the boundary along all the boundaries should be zero. For example, in Section 5.3, when all the other external boundaries in the FVM region are walls where the velocities are zero, the sum of the velocity components normal to the internal coupling boundary should also be zero. In the simulation, if the non-vanishing sum is U and there are N boundary nodes, U/N is subtracted from each node at the coupling boundary. As for another condition in Section 5.2, the sum of the velocities U should be equal to a given non-zero inlet value U_g. Then, all the boundary velocities should be multiplied by a coefficient U_g/U. Without this procedure, a certain residual will exist during the following FVM procedure. Secondly, since the velocity boundaries are adopted in the FVM, the pressures at the FVM boundary are not under control and are extrapolated by the interior pressures. Therefore, only the differences in pressure are meaningful for the FVM [30]. However, the absolute values of the pressure are used in the LBM and the pressures of the two sub-regions should be matched. In the practice, the pressure difference between the two methods at the center point of the FVM coupling boundary is calculated and subtracted by the pressures at each FVM node.

(4) FVM: The FVM is adopted to reach the time point $(n+1)\Delta t^C$ with the boundary conditions.

After the above four steps, both the LBM and the FVM proceed Δt^C along the time axis. Meanwhile, both methods are only employed for one time, which save the computational time. The above four procedures are repeated until the ending time is reached.

5. Numerical examples and discussions

In this section, some examples are simulated to validate the time coupling scheme and the ROs for incompressible LBM and temperature. In the present work, all the simulations are in lattice units and $\Delta x = \Delta t = 1$ is used.

5.1. Convection–diffusion of a Gaussian pulse

In this section, the convection–diffusion of a Gaussian pulse [35] is simulated by the coupling method to validate the temperature RO and the time coupling scheme. The computational domain is a square with length $L = 50$. The domain is divided into the FVM region at left and the LBM region at right similar to Fig. 1. Both the widths of the LBM and FVM region are 27, so the overlapping region's width is 4. The τ_v and τ_k are all 0.55 in this example, so we have $v = 1/60$ and $\alpha = 1/40$. Constant velocity components $u = v = u_0$ are specified in the entire domain. As for the number of LBM steps each FVM step, we use $m = 25$.

The initial condition is given by

$$T(x,y,0) = \exp\left[-((X-0.25)^2 + (Y-0.25)^2)\right] \tag{46}$$

in which $X = x/L$ and $X = y/L$. The analytical solution corresponding to the convection–diffusion equation (3) is

$$T(x,y,t) = \frac{1}{4t^*+1}\exp\left[-\frac{1}{4t^*+1}\left((X-Ut^*-0.25)^2 + (Y-Ut^*-0.25)^2\right)\right] \tag{47}$$

where the non-dimensional variables are defined by $t^* = t\alpha/L^2$, $U = u_0 L/\alpha$.

The boundary values of T are specified according to Eq. (47) and the non-equilibrium extrapolation scheme [36] is used in all the present work as the boundary conditions for LBM.

The numerical results for $u_0 = 0.01$ after 1250 and 2500 LBM steps are drawn against the analytical results in Fig. 4. All the results agree well with each other. The temperatures of the FVM and LBM region coincide well in the overlapping region, which validate the temperature RO.

The temperature $T(25,25)$ at the center is calculated by the coupling method and its changing along with the time is shown in Fig. 5. The velocity u_0 is 0.01, 0.02 and 0.05. The analytical results are also plotted in Fig. 5. The numerical results and the analytical results fit well with each other. The largest errors are 2.6×10^{-3}, 5.9×10^{-3} and 1.5×10^{-2} corresponding to the different velocities. The above results demonstrate that the time coupling scheme is suitable for the unsteady convection–diffusion problems.

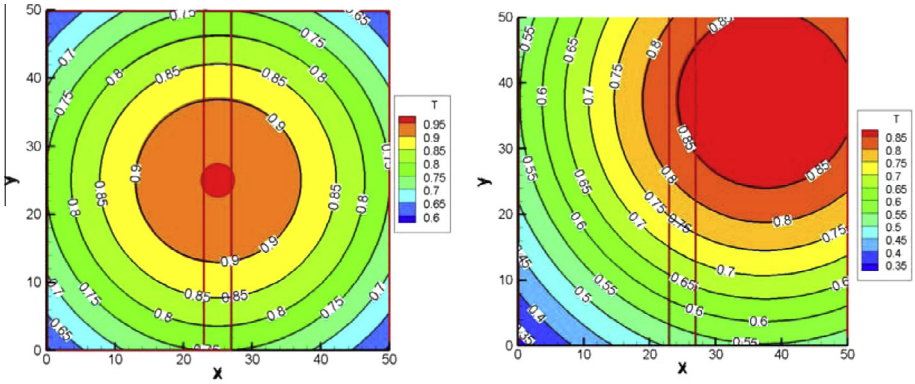

Fig. 4. The temperature contours for $u_0 = 0.01$ after 1250 and 2500 time steps (the colors are the analytical results and the lines are the numerical results). (For interpretation of the references to colour in this figure caption, the reader is referred to the web version of this article.)

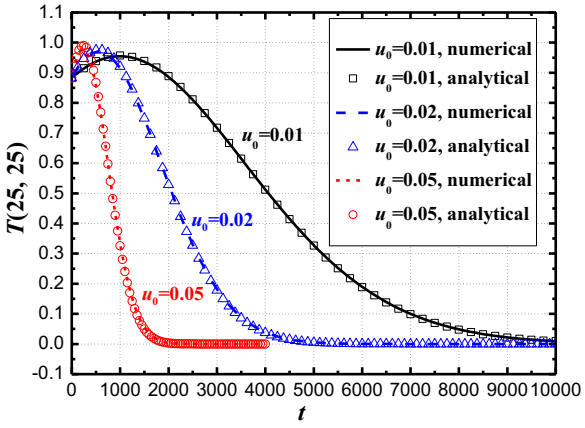

Fig. 5. The temperature $T(25,25)$ along with time, $u_0 = 0.01$, 0.02 and 0.05 (the scatters are the analytical results and the lines are the numerical results).

5.2. Flow past a circular cylinder and a porous medium

The unsteady flow around a circular cylinder is simulated in this section to validate the RO for the incompressible LBM and the unsteady scheme. The computational domain and the boundary conditions are shown in Fig. 6. The grid size is 480×210 and the widths for the left LBM region and the right FVM region are 225 and 285 separately, so the overlapping region is 30 in width. A relatively large overlapping region is used in this problem because the streamlines change sharply at the common region, and a wide buffer zone can reduce the errors in the information transfers. The velocity at the left entrance is specified as $u = u_{in} = 0.01$ and $v = 0$. At the top and bottom boundaries $v = 0$, $\partial u/\partial y = 0$ are assumed. At the right outlet boundary, the normal velocity components are calculated by the mass conservation and the tangential velocity components are calculated by the linear extrapolations of the inner velocities. The cylinder is fitted by the regular mesh. Its radius R is 15 and the center locates at (135,105). The half-way bounce-back scheme for the LBM is adopted at the boundaries. The viscosities are calculated according to the given Reynolds number $Re = u_{in}D/\nu$, in which $D = 30$ is the diameter.

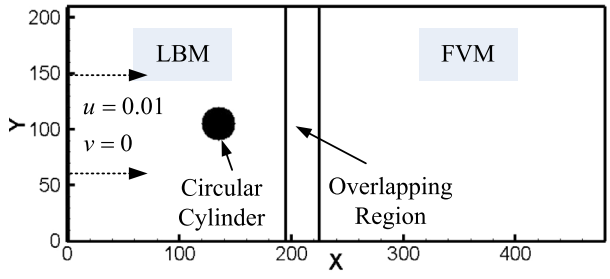

Fig. 6. The computational domain of flow past a circular cylinder.

When $Re = 300$, the streamlines at three different time steps 2.7×10^5, 3.6×10^5 and 4.5×10^5 are drown in Fig. 7. The streamlines coincide well in the overlapping region, which validate the RO for incompressible LBM.

The lift coefficient C_L is calculated by the following equation

$$C_{\mathrm{L}} = \frac{1}{u_{\mathrm{in}}^2 R}\int(-Pn_y + \nu S_{y\alpha}n_\alpha)dl \tag{48}$$

where $\boldsymbol{n} = (n_x, n_y)$ is the unit vector normal to the cylinder wall, S is defined by Eq. (29) and the repeated α donates the summation upon x, y directions. The integration is employed at the surface of the cylinder. The fluctuations of C_L along with time at $Re = 200$, 300 and 500 are drawn in Fig. 8. The Fig. 8 shows that C_L fluctuates periodically because of the creation and separation of the vortex. The Strouhal number St is defined by

$$St = fD/u_{\mathrm{in}} \tag{49}$$

in which $D = 30$ and $u_{in} = 0.01$ are given before. The vortex shedding frequency f is calculated by the fluctuations of C_L. In Fig. 8, if the time points of two wave peaks are t_1, t_2 and there are N periods between them, the frequency f is given by $N/|t_2 - t_1|$ and St is calculated by Eq. (49). The St at different Re is calculated. Since the mesh-fitting boundary is employed in the present work, the St of the present work is compared with the LBM result with non-equilibrium bounce-back scheme in Ref. [37], which can be fitted by $St = 0.24 - 0.48/Re$. Table 1 shows that the St of the present work and Ref. [37] agree well with each other. Therefore, the unsteady coupling scheme is validated.

Since the boundary condition of the cylinder is relatively simple, the FVM can also be used to simulate the flow around the cylinder. In the present work, the computational regions of FVM and LBM methods are exchanged. The velocities in the cylinder are kept to be zero when the equations of the FVM are solved. The streamlines for $Re = 300$ at different time steps are shown in Fig. 9. The streamlines in different computational regions also agree well with each other. At the same time, the streamlines in Figs. 9 and 7 are symmetric to each other with respect to the horizontal centerline. This difference may be caused by the instability when the vortex street begins.

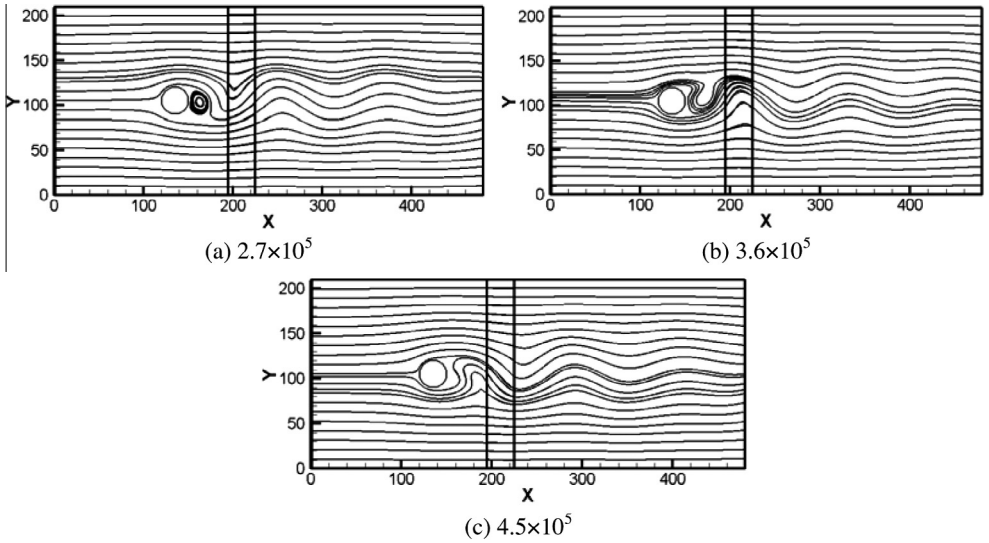

Fig. 7. The streamlines for $Re = 300$ at time steps 2.7×10^5, 3.6×10^5 and 4.5×10^5 (LBM for the near-cylinder-region).

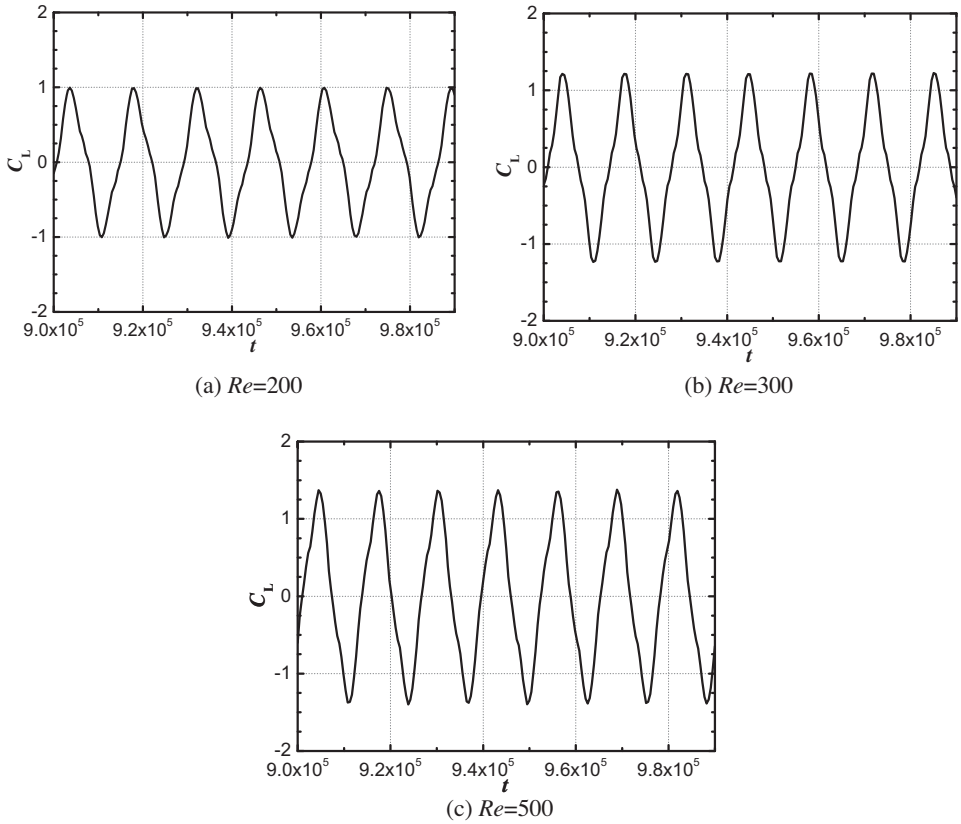

Fig. 8. The fluctuation of C_L along with time at $Re = 200$, 300 and 500.

Table 1
The *St* at different *Re*.

Re	*St* (present work)	*St* (Ref. [37])
200	0.2105	0.2140
300	0.2222	0.2240
500	0.2326	0.2310

In order to show the application of the coupling method and give a better explanation of the idea "Solving regionally and coupling at the interface", the flow past a porous medium is simulated by the coupling method. The computational domain is shown in Fig. 10. The LBM is used in the left sub-region which contains the porous medium and the FVM is used in the right sub-region. The grid size is 900×420 and the width of the LBM region is 450. The overlapping region is 30 in width. The porous medium is generated by the quartet structure generation set method [38] in the square region $200 \leqslant x \leqslant 280$, $170 \leqslant y \leqslant 250$. The porosity is 0.8. The boundary conditions are the same with the flow past a cylinder and the half-way bounce-back scheme is used at the boundaries of the porous medium. The inlet velocity is 0.01 and the viscosity is

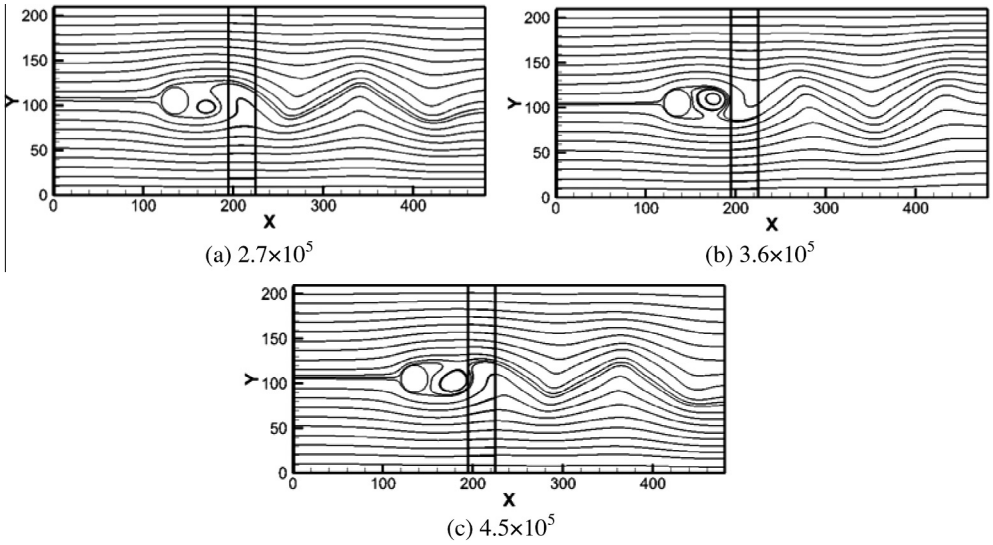

Fig. 9. The streamlines for $Re = 300$ at time steps 2.7×10^5, 3.6×10^5 and 4.5×10^5 (FVM for the near-cylinder-region).

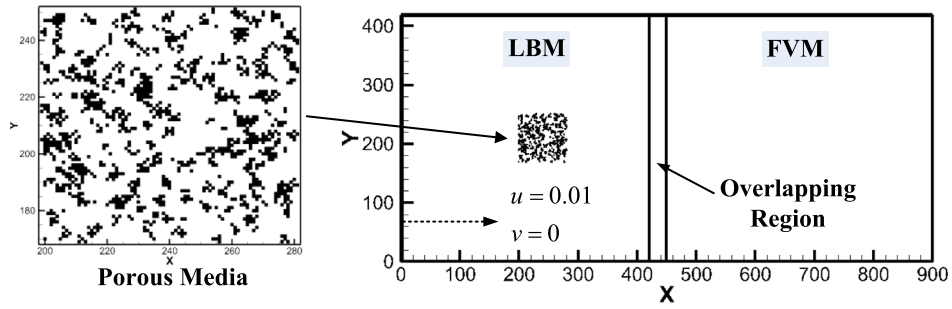

Fig. 10. The computational domain of the flow past a porous medium.

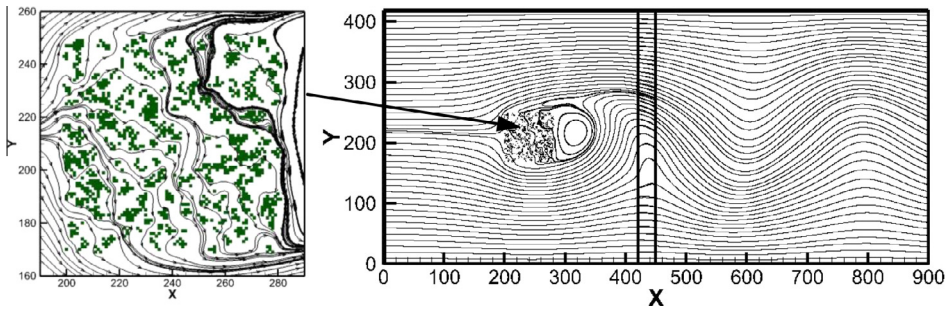

Fig. 11. The streamlines around the porous medium and the detailed streamlines within the porous medium at time step 6.3×10^5.

determined by the $Re = u_{in}D/\nu$, in which $D = 80$. In this example, we set $Re = 300$. The numerical result after 6.3×10^5 is shown in Fig. 11. The results in the two sub-regions fit well with each other and the LBM can give the detailed flow information in the porous medium. In order to further show the efficiency of the coupling method, this example is also solved by single LBM and FVM separately. Since the flow in the porous medium is hard to be simulated by FVM, instead, a square cylinder is placed at the porous area. The CPU times of the three methods are shown in Fig. 12. It can be seen that the FVM method is much faster than the other two methods, but it is hard to give the detailed flow information. Therefore, the LBM is needed, but its CPU time is relatively longer. The unsteady coupling method takes advantage of the two methods. By the coupling method, the problem can be solved within relatively shorter CPU time, and the detailed flow field can be obtained. Here we touch the core idea of the coupling strategy: the most proper numerical method should be used for different sub-processes.

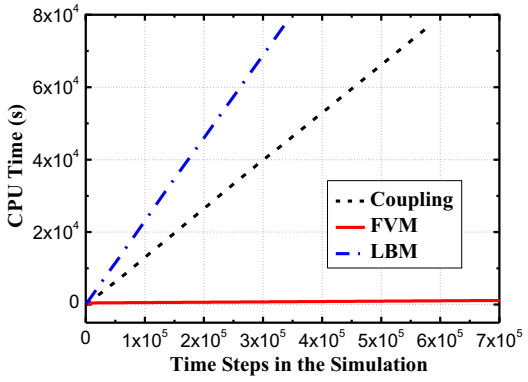

Fig. 12. The CPU times for flow past porous medium solved by coupling method, FVM and LBM.

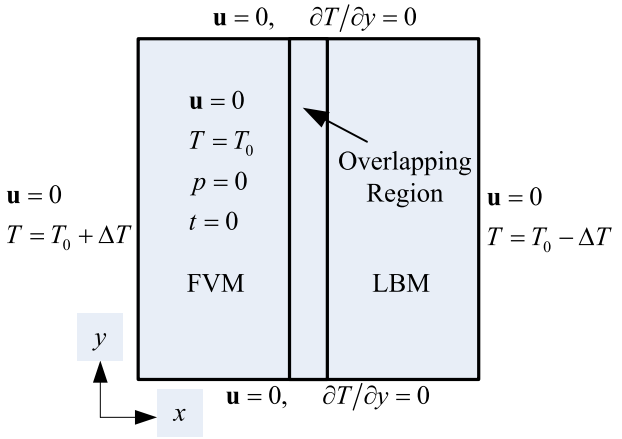

Fig. 13. The computational domain and the boundary conditions of the natural convection in a square cavity.

5.3. Unsteady natural convection in a square cavity

In this section, the start-up of the natural convection in a square cavity is simulated by the coupling method. The Boussinesq approximation is used to deal with the buoyant force, so the following external force is added to the right-hand-side of the momentum equation (2):

$$\mathbf{F} = -\mathbf{g}\beta(T - T_0) \tag{50}$$

Here $\mathbf{g}$ is the vector of the acceleration of gravity with a downwards direction, β is the coefficient of thermal expansion and T_0 is the reference temperature. As for the LBM model, the following term is added to the right-hand-side of the evolution equation (4) [26]:

$$\begin{cases} F_i = -\frac{\mathbf{e}_i \cdot \mathbf{g}}{2c^2}\beta(T - T_0), & i = 2, 4 \\ F_i = 0, & \text{other } i \end{cases} \tag{51}$$

The computational domain and the boundary conditions are shown in Fig. 13. At the beginning, the velocity and pressure in the entire area are set to zero and the temperature is the reference

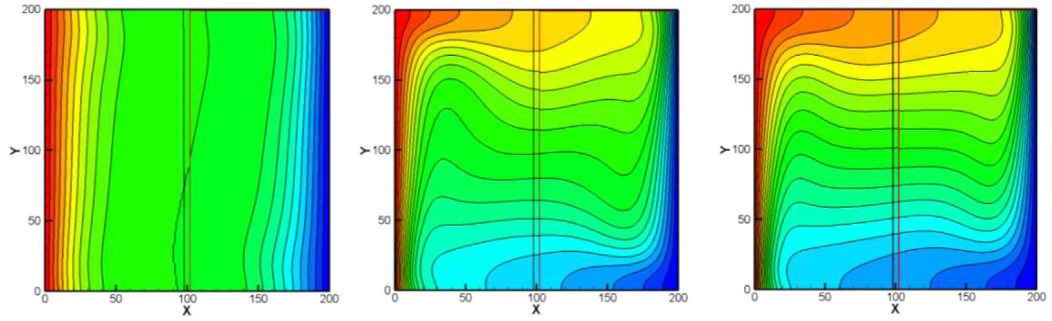

(a) The temperature distributions after 5×10^4, 1.0×10^5 and 4.8×10^5 steps (from left to right)

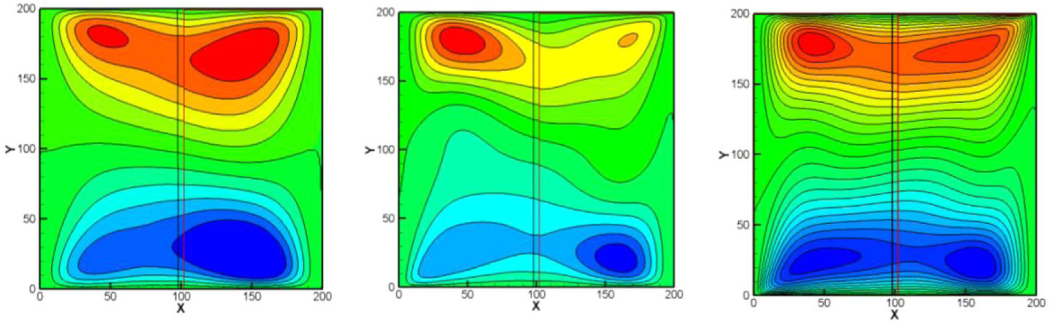

(b) The u-velocity distributions after 5×10^4, 1.0×10^5 and 4.8×10^5 steps (from left to right)

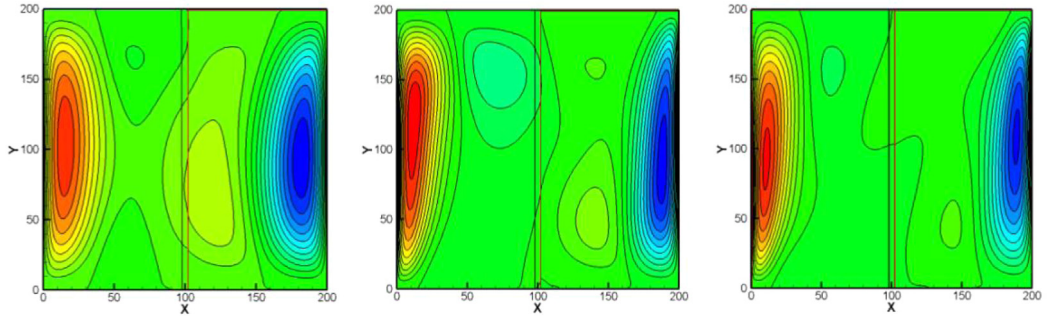

(c) The v-velocity distributions after 5×10^4, 1.0×10^5 and 4.8×10^5 steps (from left to right)

Fig. 14. The simulation results of the coupling method for $Pr = 2$ and $Ra = 1.4 \times 10^5$ after 5×10^4, 1.0×10^5 and 4.8×10^5 LBM steps.

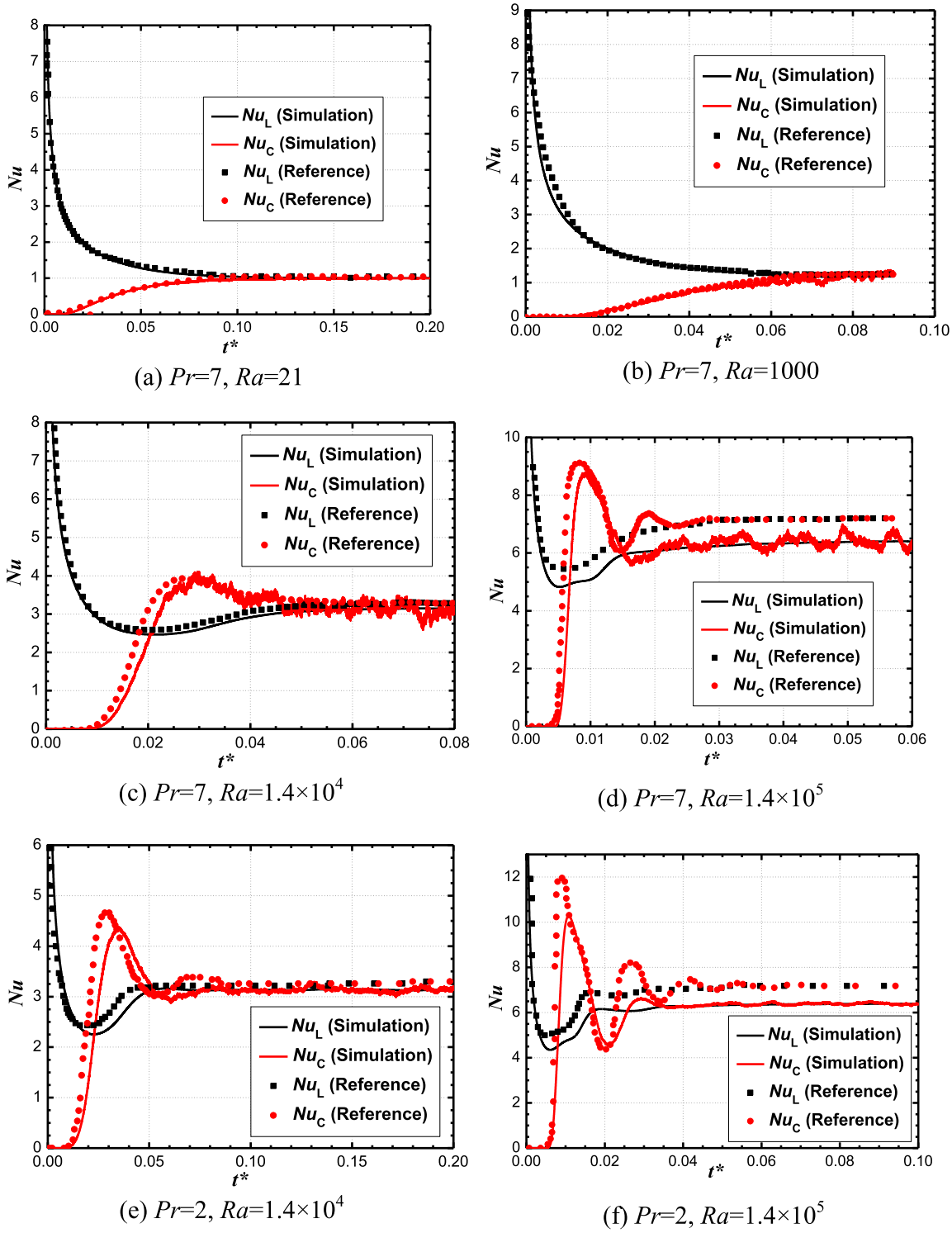

Fig. 15. The time evolution of the *Nu* for different *Pr* and *Ra* (the lines are the simulation results of the present work and the solid points are the results of Ref. [39]).

temperature. The four boundaries are non-slip walls. The top and bottom boundaries are adiabatic while the left and right boundaries are isothermal with given temperatures $T_0 + \Delta T$ and $T_0 - \Delta T$.

The grid size of the whole computational domain is 200×200. The length of the FVM region is 102 and the length of the overlapping region is 4. Therefore, the length of the LBM region is 102. We choose $m = 100$. The LBM will evolve 100 times between each FVM step. $\tau_v = 0.55$ is used so the viscosity is $v = 1/60$. The thermal diffusivity α is determined by the Prandtl number $Pr = v/\alpha$ and τ_k is therefore calculated by Eq. (13). The value of $\mathbf{g}\ \beta$ is determined by the given Rayleigh number *Ra* as

$$Ra = \frac{g\beta H^3 \Delta T}{\alpha v} \tag{52}$$

In the present work, we use $T_0 = 300$ and $\Delta T = 50$.

The simulation results for $Pr = 2$ and $Ra = 1.4 \times 10^5$ after 5×10^4, 1.0×10^5 and 4.8×10^5 LBM steps are shown in Fig. 14. The velocities and the temperatures calculated by the FVM and

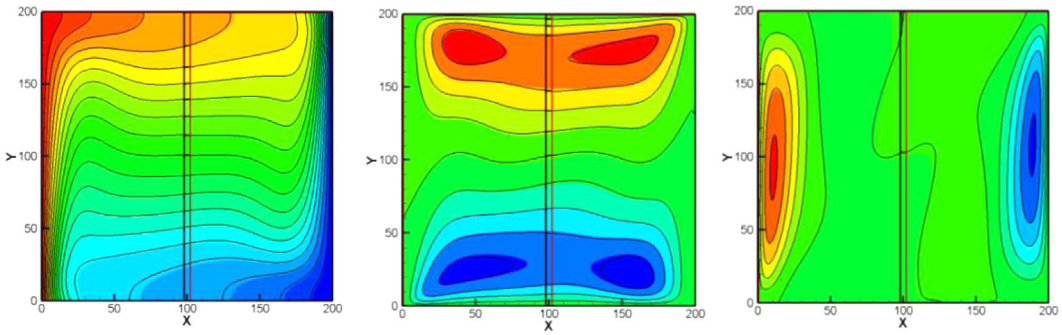

Fig. 16. The simulation results for $Pr = 2$ and $Ra = 1.4 \times 10^5$ when the steady state is reached. The simulation results are compared with the results of the FLUENT software (the colors are the FLUENT's results and the lines are the results of the coupling method). (For interpretation of the references to colour in this figure caption, the reader is referred to the web version of this article.)

LBM coincide well with each other and change smoothly through the overlapping region. Therefore, our ROs are suitable for the information transfer from LBM to FVM.

The instantaneous Nusselt numbers Nu is also calculated in the present work, which is defined by the following equations [39]:

$$Nu = \frac{1}{2}\int_0^1 \left(PrUT^* - \frac{\partial T^*}{\partial X}\right)_X dY \tag{53}$$

in which the parameters are non-dimensionalized by the following expressions.

$$\begin{aligned} &X = x/H, \quad Y = y/H \\ &U = uH/v \\ &T^* = (T - T_0)/\Delta T \\ &t^* = t\alpha/H^2 \end{aligned} \tag{54}$$

In the present work, the Nu_L at the left boundary ($X = 0$) and the Nu_C at the center line ($X = 100$) are calculated along with the time. The Nu_L and Nu_C for different Pr and Ra are plotted against the time in Fig. 15 and the results are compared with the simulation results in Ref. [39]. From Fig. 15 we can find that the results of the coupling method coincide well with Ref. [39]. The oscillations occur at almost the same time. The oscillations of the Nu_C at the center line turn to increase as the Ra increase and Pr decrease. When Ra is high, the Nu in the present work is smaller than Ref. [39] as shown in Fig. 15(d) and (f). In order to further prove the present method, the steady state results at the final moment are compared with the results solved by the FLUENT software. In Fig. 16, the velocity and temperature distributions in our simulation coincide well with the results of the FLUENT software. Therefore, our simulation results are also acceptable.

The above simulations of the unsteady square cavity natural convections demonstrate that the coupling scheme in the present work can be used to simulate the unsteady fluid flow and heat transfer problems.

6. Conclusion

In the above sections, the three shortages of the existing coupling methods have been improved.

(1) The generalized form of the RO has been introduced, which is based on the common forms of the evolution equation and distribution functions of the LBM. No premise about a special LBM model is assumed. Therefore, this generalized form is convenient for the derivation of the RO for different LBM. The existing ROs are also derived from this generalized form as the examples and validations.

(2) The RO for incompressible LBM has been obtained from the generalized RO. Therefore, the inconsistency between the density change in the LBM and the incompressible FVM has been prevented. The expression of this RO also shows that the time derivatives can simplify the RO. This RO is suitable for the coupling simulation of the incompressible flow.

(3) The unsteady coupling scheme has been described. The evolution of the LBM is considered as a natural clock. The LBM and FVM are solving sequentially and the information is transferred by the RC/CO at the intervals. Since many problems are unsteady in nature, this unsteady coupling scheme can expand the field of application of the coupling method.

Both the RO and the unsteady coupling scheme have been validated by three numerical examples: the convection–diffusion of a Gaussian pulse, the unsteady flow past a circular cylinder and the start-up processes of the natural convection in a square cavity. The simulation results agree well with the existing researches. The flow past a porous medium is also simulated as an example. The coupling method can give the detailed flow information and save the computational time.

Based on the present work, the LBM and FVM have been coupled on a more general level. Different LB model can be chosen according to the specific problem and the RO can be derived from the generalized form. Then, the LBM provides the flexibility to describe the detailed information in the regions with complex boundary or multi-physicochemical reactions [20]. The FVM can be used in other regions to save the computational time [5]. Therefore, the proposed coupling scheme is suitable for dealing with the multi-scale processes, and the further application will be reported later.

Conflict of interest

None declared.

Acknowledgments

This work is supported by the Key Project of National Natural Science Foundation of China (No. 51436007) and the National Key Basic Research Program of China (973 Program) (2013CB228304).

References

[1] K.N. Grew, W.K.S. Chiu, A review of modeling and simulation techniques across the length scales for the solid oxide fuel cell, J. Power Sources 199 (2012) 1–13.
[2] C.R. Kleijn, R. Dorsman, K.J. Kuijlaars, M. Okkerse, H. van Santen, Multi-scale modeling of chemical vapor deposition processes for thin film technology, J. Crystal Growth 303 (1) (2007) 362–380.

[3] J.Q. Shi, S. Durucan, A bidisperse pore diffusion model for methane displacement desorption in coal by CO_2 injection, Fuel 82 (10) (2003) 1219–1229.
[4] T. Xie, Y.L. He, Z.J. Hu, Theoretical study on thermal conductivities of silica aerogel composite insulating material, Int. J. Heat Mass Transfer 58 (1–2) (2013) 540–552.
[5] H.B. Luan, H. Xu, L. Chen, D.L. Sun, W.Q. Tao, Numerical Illustrations of the coupling between the lattice Boltzmann method and finite-type macro-numerical methods, Numer. Heat Transfer Part B-Fundam. 57 (2) (2010) 147–171.
[6] B. Engquist, P. Lötstedt, O. Runborg, Multiscale Modeling and Simulation in Science, Springer, Berlin/Heidelberg, 2009.
[7] Y.L. He, W.Q. Tao, Multiscale simulations of heat transfer and fluid flow problems, J. Heat Transfer 134 (3) (2012) 031018.
[8] S.T. O'Connell, P.A. Thompson, Molecular dynamics-continuum hybrid computations: a tool for studying complex fluid flows, Phys. Rev. E 52 (6) (1995) R5792–R5795.
[9] E.G. Flekkoy, G. Wagner, J. Feder, Hybrid model for combined particle and continuum dynamics, Europhys. Lett. 52 (3) (2000) 271–276.
[10] X.B. Nie, S.Y. Chen, W.N. E, M.O. Robbins, A continuum and molecular dynamics hybrid method for micro- and nano-fluid flow, J. Fluid Mech. 500 (2004) 55–64.
[11] J. Sun, Y.L. He, W.Q. Tao, Molecular dynamics-continuum hybrid simulation for condensation of gas flow in a microchannel, Microfluid. Nanofluid. 7 (3) (2009) 407–422.
[12] J. Sun, Y.L. He, W.Q. Tao, Scale effect on flow and thermal boundaries in micro-/nano-channel flow using molecular dynamics-continuum hybrid simulation method, Int. J. Numer. Methods Eng. 81 (2) (2010) 207–228.
[13] J. Sun, Y.L. He, W.Q. Tao, X. Yin, H.S. Wang, Roughness effect on flow and thermal boundaries in microchannel/nanochannel flow using molecular dynamics-continuum hybrid simulation, Int. J. Numer. Methods Eng. 89 (1) (2012) 2–19.
[14] O. Aktas, N.R. Aluru, A combined continuum/DSMC technique for multiscale analysis of microfluidic filters, J. Comput. Phys. 178 (2) (2002) 342–372.
[15] T.E. Schwartzentruber, L.C. Scalabrin, I.D. Boyd, A modular particle-continuum numerical method for hypersonic non-equilibrium gas flows, J. Comput. Phys. 225 (1) (2007) 1159–1174.
[16] H.B. Luan, H. Xu, L. Chen, Y.L. Feng, Y.L. He, W.Q. Tao, Coupling of finite volume method and thermal lattice Boltzmann method and its application to natural convection, Int. J. Numer. Methods Fluids 70 (2) (2012) 200–221.
[17] H.B. Luan, H. Xu, L. Chen, D.L. Sun, Y.L. He, W.Q. Tao, Evaluation of the coupling scheme of FVM and LBM for fluid flows around complex geometries, Int. J. Heat Mass Transfer 54 (9–10) (2011) 1975–1985.
[18] L. Chen, H.B. Luan, Y.L. Feng, C.X. Song, Y.L. He, W.Q. Tao, Coupling between finite volume method and lattice Boltzmann method and its application to fluid flow and mass transport in proton exchange membrane fuel cell, Int. J. Heat Mass Transfer 55 (13–14) (2012) 3834–3848.
[19] L. Chen, Y.L. Feng, C.X. Song, L. Chen, Y.L. He, W.Q. Tao, Multi-scale modeling of proton exchange membrane fuel cell by coupling finite volume method and lattice Boltzmann method, Int. J. Heat Mass Transfer 63 (2013) 268–283.
[20] L. Chen, Y.L. He, Q. Kang, W.Q. Tao, Coupled numerical approach combining finite volume and lattice Boltzmann methods for multi-scale multi-physicochemical processes, J. Comput. Phys. 255 (2013) 83–105.
[21] H. Xu, H.B. Luan, Y.L. He, W.Q. Tao, A lifting relation from macroscopic variables to mesoscopic variables in lattice Boltzmann method: derivation, numerical assessments and coupling computations validation, Comput. Fluids 54 (2012) 92–104.
[22] Z.X. Tong, Y.L. He, L. Chen, T. Xie, A multi-component lattice Boltzmann method in consistent with Stefan–Maxwell equations: derivation, validation and application in porous medium, Comput. Fluids 105 (2014) 155–165.
[23] S. Gong, P. Cheng, Lattice Boltzmann simulation of periodic bubble nucleation, growth and departure from a heated surface in pool boiling, Int. J. Heat Mass Transfer 64 (2013) 122–132.
[24] S. Chen, G.D. Doolen, Lattice Boltzmann method for fluid flows, Annu. Rev. Fluid Mech. 30 (1998) 329–364.
[25] Z. Guo, B. Shi, N. Wang, Lattice BGK model for incompressible Navier–Stokes equation, J. Comput. Phys. 165 (1) (2000) 288–306.
[26] Z. Guo, B. Shi, C. Zheng, A coupled lattice BGK model for the Boussinesq equations, Int. J. Numer. Methods Fluids 39 (4) (2002) 325–342.
[27] P.K. Kundu, I.M. Cohen, Fluid Mechanics, fourth ed., Academic, Burlington, 2008.
[28] R. Delgado-Buscalioni, P.V. Coveney, Hybrid molecular-continuum fluid dynamics, Philos. Trans. R. Soc. London Ser. A: Math. Phys. Eng. Sci. 362 (1821) (2004) 1639–1654.
[29] Y.C. Wang, G.W. He, A dynamic coupling model for hybrid atomistic-continuum computations, Chem. Eng. Sci. 62 (13) (2007) 3574–3579.
[30] S.V. Patankar, Numerical Heat Transfer and Fluid Flow, McGraw-Hill, New York, 1980.
[31] W.Q. Tao, Numerical Heat Transfer, second ed., Xi'an Jiaotong University Press, Xi'an, 2001 (in Chinese).
[32] Y.H. Qian, D. Dhumieres, P. Lallemand, Lattice BGK models for Navier–Stokes equation, Europhys. Lett. 17 (6) (1992) 479–484.
[33] R.R. Nourgaliev, T.N. Dinh, T.G. Theofanous, D. Joseph, The lattice Boltzmann equation method: theoretical interpretation, numerics and implications, Int. J. Multiphase Flow 29 (1) (2003) 117–169.
[34] Y.L. He, Y. Wang, Q. Li, Lattice Boltzmann Method: Theory and Application, Science Press, Beijing, 2009 (in Chinese).
[35] J.C. Kalita, D.C. Dalal, A.K. Dass, A class of higher order compact schemes for the unsteady two-dimensional convection–diffusion equation with variable convection coefficients, Int. J. Numer. Methods Fluids 38 (12) (2002) 1111–1131.
[36] Z.L. Guo, C.G. Zheng, B.C. Shi, Non-equilibrium extrapolation method for velocity and pressure boundary conditions in the lattice Boltzmann method, Chin. Phys. 11 (4) (2002) 366–374.
[37] A. Grucelski, J. Pozorski, Lattice Boltzmann simulations of flow past a circular cylinder and in simple porous media, Comput. Fluids 71 (2013) 406–416.
[38] M. Wang, J. Wang, N. Pan, S.Y. Chen, Mesoscopic predictions of the effective thermal conductivity for microscale random porous media, Phys. Rev. E 75 (3) (2007) 036702.
[39] J. Patterson, J. Imberger, Unsteady natural convection in a rectangular cavity, J. Fluid Mech. 100 (1) (1980) 65–86.